Dielectric function in the NIR-VUV spectral range of $(In_xGa_{1-x})_2O_3$ thin films

R. Schmidt-Grund, C. Kranert, T. Böntgen, H. von Wenckstern, H. Krauß, and M. Grundmann

Citation: Journal of Applied Physics **116**, 053510 (2014); doi: 10.1063/1.4891521
View online: https://doi.org/10.1063/1.4891521
View Table of Contents: http://aip.scitation.org/toc/jap/116/5
Published by the American Institute of Physics

JOURNAL OF APPLIED PHYSICS **116**, 053510 (2014)

Dielectric function in the NIR-VUV spectral range of $(In_xGa_{1-x})_2O_3$ thin films

R. Schmidt-Grund,[a] C. Kranert, T. Böntgen, H. von Wenckstern, H. Krauß, and M. Grundmann

Fakultät für Physik und Geowissenschaften, Institut für Experimentelle Physik II, Universität Leipzig, Linnéstr. 5, D-04103 Leipzig, Germany

(Received 19 June 2014; accepted 17 July 2014; published online 4 August 2014)

We determined the dielectric function of the alloy system $(In_xGa_{1-x})_2O_3$ by spectroscopic ellipsometry in the wide spectral range from 0.5 eV to 8.5 eV and for In contents ranging from $x = 0.02$ to $x = 0.61$. The predicted optical transitions for binary, monoclinic β-Ga_2O_3, and cubic bcc-In_2O_3 are well reflected by the change of the dielectric functions' lineshape as a function of the In content. In an intermediate composition range with phase-separated material ($x \approx 0.3 \ldots 0.4$), the lineshape differs considerably, which we assign to the presence of the high-pressure rhombohedral $InGaO_3$-II phase, which we also observe in Raman experiments in this range. By model analysis of the dielectric function, we derived spectra of the refractive index and the absorption coefficient and energy parameters of electronic band-band transitions. We discuss the sub-band gap absorption tail in relation to the influence of the In 4*d* orbitals on the valence bands. The data presented here provide a basis for a deeper understanding of the electronic properties of this technologically important material system and may be useful for device engineering. © *2014 AIP Publishing LLC*.
[http://dx.doi.org/10.1063/1.4891521]

I. INTRODUCTION

Due to its large band gap between approximately 3.5 eV and 5 eV, the alloy system $(In_xGa_{1-x})_2O_3$ can be promising for use in applications like high-power devices, transparent electronics, and solar-blind ultraviolet (UV) photo-detectors.[1] Fabrication of such devices requires knowledge of basic properties of this material like the dielectric function (DF) and absorption coefficient as well as of the electronic band structure. In the last years, binary Ga_2O_3 and In_2O_3 and recently also their ternary alloys have come in focus of research. But detailed knowledge of properties of the dielectric function and band-band transitions is missing so far. In this work, we present spectra of the dielectric function for a large composition range $x = 0.02-0.61$ and for energies (0.5–8.5) eV determined by spectroscopic ellipsometry. We discuss their lineshape in comparison with theoretical predictions. By a lineshape model analysis of the DF, we obtain further spectra of the refractive index and absorption coefficient and derive energy parameters of band-band transitions.

In the following, we review theoretical predictions and experimental observations of optical and electronic band structure properties. Then, we introduce the experimental details in Sec. II, followed by the discussion of the dielectric function properties in Sec. III.

The electronic and optical properties in the near-infrared to vacuum-ultraviolet spectral range of different polymorphs of Ga_2O_3 and In_2O_3 have been thoroughly studied theoretically[2–10] but less comprehensively by experiment.[10–19] For the $(In_xGa_{1-x})_2O_3$ alloy system, only few experimental reports on optical properties are available limited to transmission investigations of the band gap properties.[20,21] In the following, we restrict the discussion to the polymorphs relevant for this work: β-Ga_2O_3 (monoclinic) and bcc-In_2O_3 (cubic), and shortly introduce some properties of rh-In_2O_3 (rhombohedral). Please note, in literature, these phases are often labelled In_2O_3-II for bcc-In_2O_3 and In_2O_3-III for rh-In_2O_3. For the high-pressure rhombohedral $InGaO_3$-II, which is present in our films in an intermediate composition range (c.f. Ref. 22), no optical or band structure properties are available. It shall be mentioned that the two rhombohedral phases not only differ in stoichiometry, but are two different crystal structures with regard to yet known structural and phonon mode properties.[22–25]

The highest valence bands of β-Ga_2O_3 consist mainly of O 2*p* orbitals,[2–4] which for bcc- and rh-In_2O_3 are hybridized with In 4*d* (Refs. 5–7)/In 5*p* (Ref. 9) orbitals. Also In 4*d*-O 2*s* hybridization was reported.[10] The admixture of the In 4*d* orbitals is claimed to be responsible for a dipole forbidden direct band gap and/or an indirect band gap.[5–7,10] The lowest conduction bands of β-Ga_2O_3 are mainly due to Ga 4*s* orbitals. Those of bcc-In_2O_3 are claimed to consist of In 5*s* and In 5*p* (Ref. 6) or In 5*s* hybridized with O 2*s* (Refs. 5 and 9), while those of rh-In_2O_3 are predicted to be mainly In 5*s* orbitals.[5] Thus, for the $(In_xGa_{1-x})_2O_3$ alloy, the optical band-band transitions in the vicinity of the fundamental band gap are expected to be influenced by the following reasons: (i) The admixture of the In 4*d* orbitals in the mainly O 2*p* like valence bands should cause a widening of the sub-band gap absorption tail. (ii) The substitution of Ga- by In-related orbitals in the conduction bands should have the strongest influence on the energetic positions of the optical transitions. (iii) Due to the very similar orbital structure of both end components, a smooth evolution of the optical properties by replacing the metal ions is expected.

[a]Schmidt-Grund@physik.uni-leipzig.de

Comparing the theoretically predicted spectra of the complex DF $\tilde{\varepsilon}$ (Refs. 3–6), some distinct changes of the lineshape within the alloy system are expected. While the imaginary part ε_2 for β-Ga_2O_3 yields the strongest absorption between 10 eV and 17 eV, for bcc-In_2O_3, the strongest absorption is predicted at lower energies between 8 eV and 14 eV, reflecting also the redshift of the band gap energy. Comparing the real part of the DF ε_1 of both, considerable differences in the lineshape are recognisable. While for β-Ga_2O_3, ε_1 is almost constant between the band gap energy and 10 eV, a strong decrease is predicted for bcc-In_2O_3 for energies above the band gap. For rh-In_2O_3, the situation is quite different:[5] ε_2 shows additionally a strong peak around 8 eV and ε_1 does not decrease as fast as for In_2O_3-II at energies above the band gap but rather increases again up to 8 eV. Please note that we do not discuss the anisotropy of the optical properties because we have, due to the crystalline structure of our films, no access to the tensor elements of $\tilde{\varepsilon}$ (c.f. also Sec. II B).

Experimentally, the near band gap optical properties of β-Ga_2O_3, bcc-In_2O_3, and $(In_xGa_{1-x})_2O_3$ single crystals and thin films deposited on different substrates in the spectral range 0.75–6 eV have mainly been investigated by means of transmission experiments (yielding the transmittance T),[10–17,20,21] but also ellipsometric investigations are reported.[18,19] Energies of the band gap, partially for two of the principal tensor components of $\tilde{\varepsilon}$, and spectra of the absorption coefficient α as well as the complex refractive index $\tilde{n} = n + ik$ have been derived. Spectra of $\tilde{\varepsilon}$ have not been reported. Room temperature values of the band gap(s) in the range 4.5…4.9 eV for Ga_2O_3 and 3.55…3.84 eV for the direct respective 2.62…2.93 eV for the indirect or dipole forbitten direct transition for In_2O_3 have been found.[10–19] For the $(In_xGa_{1-x})_2O_3$ alloy system, with increasing x a shift of the absorption edge from 4.46 eV to 3.72 eV (Ref. 21) with a pronounced bowing within the entire composition range and from 5.0 eV to 4.0 eV (Ref. 20) for films up to $x = 0.35$ with the occurrence of phase separation for $x > 0.08$ have been reported. In general, all spectra of α, $\tilde{n}$, and T show pronounced absorption tails below the band gap, which extend as wide as up to 1 eV.

II. EXPERIMENTAL DETAILS

A. Samples

The $(In_xGa_{1-x})_2O_3$ thin film samples with continuous composition spread (CCS) have been grown by means of pulsed laser deposition (PLD) using a segmented PLD target (for further details on the CCS technique, see von Wenckstern *et al.*[26]). We used 2-in. wafers of (00.1)-oriented α-Al_2O_3 and (100)-oriented MgO as substrates. More details on the growth conditions can be found in Ref. 22. As also detailed in Ref. 22, the composition as a function of the position on the wafer and the structural properties of the thin films have been investigated by means of energy dispersive X-Ray analysis (EDX), X-Ray diffraction (XRD), and Raman spectroscopy. Figure 1 displays EDX line scans of the In concentration of the samples. For low In concentration, we found full incorporation of In in the Ga_2O_3-lattice and thus single phase material. This part of the films is found to be $(\bar{2}01)$-oriented on the Al_2O_3 and (100)-oriented on the MgO substrate. For In concentration higher than ≈0.2 (Al_2O_3 substrate[34] and ≈0.3 (MgO substrate), we found phase separation, namely, the occurrence of the high-pressure $InGaO_3$-II phase and for $x > 0.6$ (111)-oriented bcc-In_2O_3 within the (100)- as well as (111)-oriented $(In_xGa_{1-x})_2O_3$ host material. We found that the change of lattice parameters is strongest in between the monoclinic and the cubic phases. The position of the phonon modes is basically linearly dependent on the composition but new Raman features arise in some composition ranges, which can be ascribed to the different crystallographic phases.

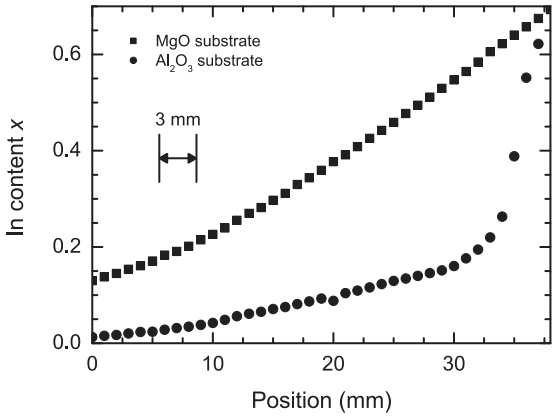

FIG. 1. EDX line scans of the indium concentration x of the CCS samples along the positions of the ellipsometry measurements (squares: MgO substrate, circles: Al_2O_3 substrate). The spatial resolution (≈3 mm) of the ellipsometry measurement is indicated.

B. Spectroscopic ellipsometry

The dielectric functions of the thin films have been determined by means of standard spectroscopic ellipsometry[27] in a wide spectral range from 0.5 to 8.45 eV at room temperature using a commercial spectroscopic ellipsometer. The measurements were carried out along the In gradient every 3 mm from edge to edge. Here, the light propagation direction was perpendicular to the In gradient and the spot size on the sample approximately 3 mm in width and 5 mm long. Thus, for each measurement, a range of typically $\Delta x \approx 0.03$ with different In concentrations, depending on the position on the sample, is probed (Fig. 1).

In ellipsometry, the change of the polarization state of a light beam after interaction with a sample is measured. In the simplest case of optically (effective) isotropic and non-depolarizing materials respective samples, this can be expressed by the ratio $\tilde{\rho} = \tilde{r}_p/\tilde{r}_s$ of the complex reflection coefficients $\tilde{r}_i$ for light polarized parallel (i = p) and perpendicular (i = s) to the plane of incidence, which is spanned by the beam direction and the samples' surface normal. The measured quantities can be expressed by the pseudo dielectric function:

$$\langle\tilde{\varepsilon}\rangle = \langle\varepsilon_1\rangle - i\langle\varepsilon_2\rangle = \sin^2\phi\left[1 + \tan^2\phi\left(\frac{1-\tilde{\rho}}{1+\tilde{\rho}}\right)^2\right], \quad (1)$$

where ϕ is the angle of incidence. In case of a half infinite single phase, optically isotropic bulk sample $\tilde{\rho}$ is directly connected to the real and imaginary parts of the complex reflectivity and thus to the materials' complex DF $\tilde{\varepsilon} = \varepsilon_1 + i\varepsilon_2$ and $\langle\tilde{\varepsilon}\rangle \equiv \tilde{\varepsilon}$. In any other case, a model analysis of the experimental data has to be done to extract the materials' DFs and layer thicknesses.

The experimental data are analysed using a transfer-matrix technique[27] with matrices for each layer of the sample stack: half-infinite Al_2O_3 or MgO substrate, the thin film of interest and surface roughness. The substrates DF were determined previously. The DFs of the materials were described by either analytic, line-shape function based parametric model-DFs (MDF, cf. Sec. III B 1) or numerically by Kramers-Kronig consistent mathematical inversion of the experimental data. The surface of the oxide thin films was assumed to show some roughness without any chemical modification; thus, a standard Bruggeman effective-medium approximation (EMA) (Ref. 28) was applied, allowing for variable fractions in mixing of the dielectric functions of the thin film and void. Regression analysis using a Levenberg-Marquardt algorithm was applied to best match the model to the experimental data.

The analysis for the $(In_xGa_{1-x})_2O_3$ was done in three steps. First, the thickness of the layers was determined by applying a Cauchy model[27] in the transparency spectral range extending up to ≈(2.5…4) eV depending on the In concentration. Then, a Kramers-Kronig consistent mathematical inversion of the experimental data was carried out using the layer thickness obtained above. Finally, the numerical DF were approximated by lineshape functions as discussed in Sec. III B 1 in order to gain physical parameters for optical transitions as a function of the In content. Examples for the model approximation to the experimental data are shown in Fig. 2.

Please note that we have determined the effective isotropic dielectric function[29] of this optically biaxial material (at least true for low In contents) because we have no access to the individual dielectric tensor components caused in rotation domains and twinning of the crystallites and the occurrence of the different crystal structure phases in the thin films. Thus, some of the individual features may belong to different tensor elements and the determined energies and the large broadening of the transitions observed may also be influenced, respectively, caused by a superposition of the response from the individual tensor elements. But the general trend in change of the lineshape and the composition evolution is considered reliable.

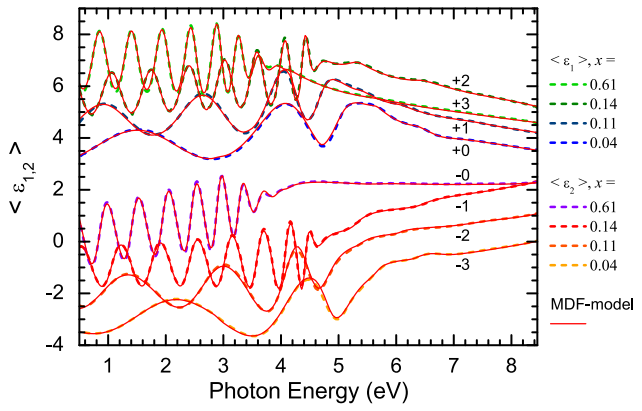

FIG. 2. Experimentally determined (dashed lines) and model calculated (red solid lines) spectra of the pseudo dielectric functions $\langle\varepsilon_{1,2}\rangle$ for selected In concentrations x for an angle of incidence of $\phi = 60°$. The spectra are shifted vertically against each other for clarity as indicated in the figure. Please note the change in the period of the layer thickness interference pattern. The thickness of the films ranges between 100 nm and 600 nm.

III. RESULTS AND DISCUSSION

A. Refractive index

All films are transparent in a wide spectral range, where the optical response is fully described by the real part of the DF or rather the refractive index $n = \sqrt{\varepsilon_1}$. The energy dispersion of n can thus be described by the so-called Cauchy model[27] as follows (valid for $\alpha < 10\,\mathrm{cm}^{-1}$, α being the absorption coefficient, cf. Fig. 5):

$$n(\lambda) = A + \frac{B}{\lambda^2} + \frac{C}{\lambda^4}, \tag{2}$$

with λ being the vacuum wavelength of light in units of μm and A, B, C adjustable parameters. Spectra of $n(E)$ are shown in Fig. 3(a) and the Cauchy parameters as a function of the composition are given in Fig. 3(b). A clear increase of $n(E)$ with increasing x can be observed.

The Cauchy parameter A can be related to the high-frequency dielectric constant by $A \equiv n_\infty = \sqrt{\varepsilon_\infty}$. Comparing the results found here to values reported in the literature, we find that for $x = 0.02$, $A \approx 1.9$ is very close to values for Ga_2O_3, which are in the range $n_\infty \approx 1.89$ (experiment[18]) and $n_\infty \approx 1.67\ldots1.69$ (theory[4]). For $x = 0.61$, $A \approx 1.99$ approaches the value for bcc-In_2O_3 of $n_\infty \approx 1.79\ldots2$ (experiment[15,19]) and $n_\infty \approx 2.0$ (theory[6]).

B. Dielectric function

Spectra of the real and imaginary parts of the dielectric function $\tilde{\varepsilon} = \varepsilon_1 + i\varepsilon_2$ and the derived absorption coefficient α for all compositions investigated are shown in Figs. 4 and 5. Strong absorption sets in at $E \approx 5\ldots3$ eV for $x = 0.02\ldots0.61$, respectively. At higher energies, several features due to electronic transitions are observable. Remarkably, different general lineshapes appear for three composition ranges respective substrate types, namely, for (I) $x = 0.02\ldots0.11$ (Al_2O_3), (II) $x = 0.14\ldots0.27$ (MgO), and (III) $x = 0.39\ldots0.61$ (MgO). For $x = 0.33$, the lineshape differs from all other and seems to be partially a mixture of those from the ranges (II) and (III), reflecting the composition range of pronounced structural changes as discussed in Sec. II A. As a general observation, the spectral broadening of the features and the overall spectral weight increases with increasing x. Further, wide sub-band gap absorption tails are observable, which are more pronounced for larger x values, reflecting small absorption by the dipole forbidden direct and/or the evolving indirect band gap due to the increasing influence of the In 4*d* orbitals on the valence bands as discussed in Sec. I.

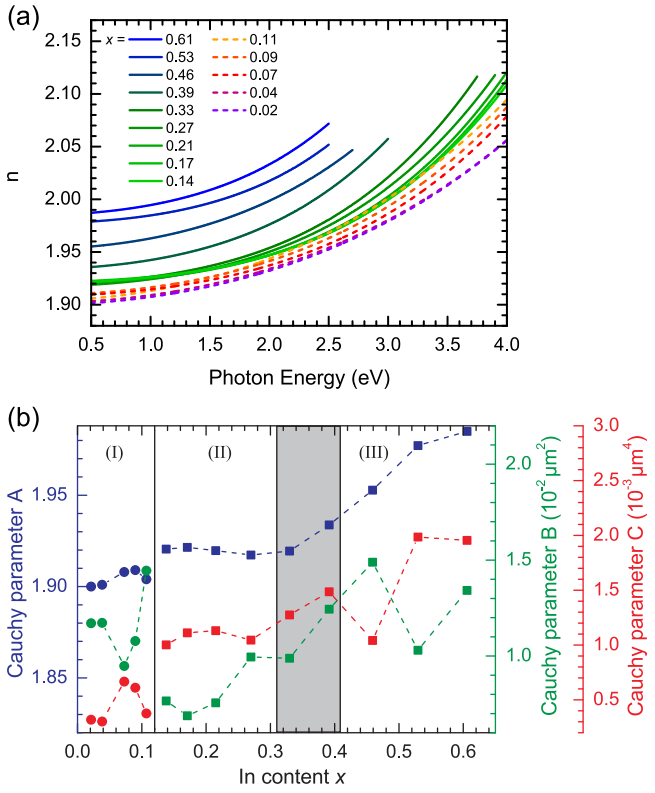

FIG. 3. (a) Spectra of the refractive index in the transparency spectral range for all x investigated. (b) Parameters of the Cauchy model (Eq. (2)) as a function of x (symbols, lines are guides to the eye only). Please note that the scatter in the parameter values can largely be attributed to pronounced correlation between the Cauchy parameters in the regression analysis. The grey marked area indicates for the sample with MgO substrate, the composition range of the transition from the single phase to the phase separated structure as significantly observable in the dielectric function spectra. In (a) and (b), solid lines/squares and dashed lines/circles indicate the thin films grown on MgO and Al_2O_3 substrates, respectively.

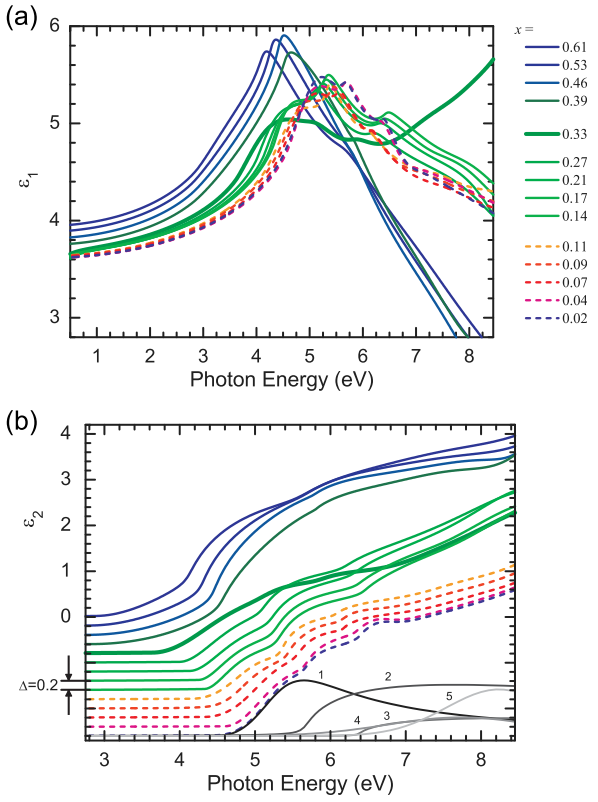

FIG. 4. Spectra of the (a) real (ε_1) and (b) imaginary parts (ε_2) of the dielectric functions for all In concentrations x. Solid and dashed lines indicate the thin films grown on MgO and Al_2O_3 substrates, respectively. For ε_2, the spectral range revealing non-vanishing values is shown only and the spectra are shifted vertically against each other for clarity as indicated. Further, the individual contributions to the model dielectric function for $x = 0.02$ are shown by grey lines (from dark to light: 1: TcLo, 2: CPM0-1, 3: CPM0-2, 4: Gaussian-1, 5: Gaussian-2).

Comparing the lineshape of the DF found here to that predicted theoretically for β-Ga_2O_3 and bcc- and rh-In_2O_3,[3–6] one finds that the general trend of the redshift of the features with increasing x reflects the transition from the β-Ga_2O_3-like lineshape to the bcc-In_2O_3-like lineshape. Generally, in ε_2, the pronounced shoulders above the fundamental band gap and the further increase towards higher energies nicely correlate. In ε_1, characteristic features due to the incorporation of In are clearly observable. Starting at $x = 0.02$, at higher energies, ε_1 yields the relatively flat lineshape of the β-Ga_2O_3-type. By increasing x within the ranges (I) and (II), features around 6…7 eV become more pronounced, which are characteristic for the bcc-In_2O_3-type lineshape, but the strong decrease of ε_1 at even higher energies does not occur. Therefore, we conclude that for $x < 0.3$, the materials' electronic structure is dominantly β-Ga_2O_3-like. For the range (III), the strong decrease of ε_1 at high energies resembles that for bcc-In_2O_3. Thus, we conclude that for $x > 0.4$, the materials' electronic structure is dominantly bcc-In_2O_3-like. The exceptional lineshape for $x = 0.33$ in the transition range between the homogeneous (ranges (I and II)) and the phase separated (range (III)) composition range shows the behaviour as predicted for rh-In_2O_3, i.e., the strong increase of ε_1 for energies up to 8 eV. In that composition range, we have found in the Raman data strong signatures of the high-pressure rhombohedral $InGaO_3$-II phase.[22] As mentioned above, from the structural point of view, this phase shows no similarity to rh-In_2O_3.[22–25] The electronic structure of $InGaO_3$-II is not known so far, but it seems that the optical response and thus also the electronic structure of that phase should be similar to that of the rh-In_2O_3 phase.

In the following, we will introduce the MDF used to describe the lineshape of $\tilde{\varepsilon}$ and discuss the composition dependence of contributions to the MDF and some of their parameters.

1. Model

The near band gap DF of direct band-gap crystalline semiconductors usually is characterized by M0-like critical point transitions and can be described by the approach by Adachi (in the following, denoted as CPM0).[30,31] We have used an exponential instead of a parabolic onset of the absorption due to the disorder in the atomic site occupation in the ternary crystal, the occurrence of different phases and/or weak absorption caused by symmetry forbidden transitions or an indirect band gap. An appropriate MDF is the Tauc-Lorentz model, which was originally developed for the description of the near band gap DF of amorphous materials.[32] It considers non-parabolic bands caused in the lack of

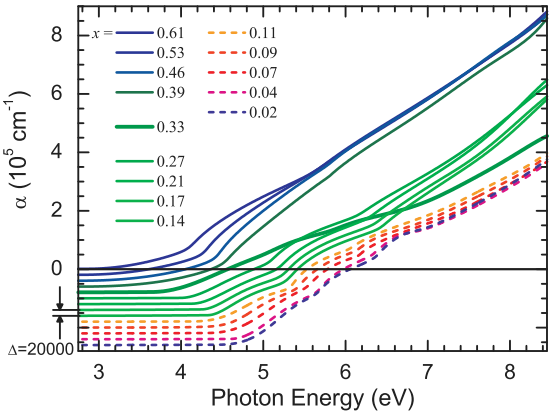

FIG. 5. Spectra of the absorption coefficient α calculated from the MDF. Solid and dashed lines indicate the thin films grown on MgO and Al_2O_3 substrates, respectively. The spectra are shifted vertically against each other for clarity as indicated.

long-range order in the crystal by replacing the parabolic onset of the absorption due to the fundamental band-band transitions by a Lorentz oscillator. The Tauc-Lorentz model for ϵ_2 usually reads[32] (ε_1 follows from the Kramers-Kronig transformation):

$$\varepsilon_{2,\mathrm{TcLo}}(E) = \begin{cases} 0 & 0 < E \le E_\mathrm{g} \\ [T(E) \cdot L(E)] & E > E_\mathrm{g}, \end{cases} \tag{3}$$

with the Tauc absorption

$$T(E) = \frac{(E - E_\mathrm{g})^2}{E^2}, \tag{4}$$

and the Lorentz oscillator

$$L(E) = \frac{A E_\mathrm{n} \Gamma E}{\left[\left(E^2 - E_\mathrm{n}^2\right)^2 + \Gamma^2 E^2\right]}, \tag{5}$$

where E is the photon energy. The energy E_g describes the usual band gap energy for parabolic bands and E_n the resonance energy of the Lorentz oscillator. A and Γ denote the amplitude and the broadening of the Lorentz oscillator. While in the case of $E_\mathrm{g} \ll E_\mathrm{n}$ and $\Gamma < E_\mathrm{n} - E_\mathrm{g}$, the spectral shape of $\varepsilon_{2,\mathrm{TcLo}}$ is dominated by the strong Lorentzian peak and a wide but weak low-energy absorption tail, which is suitable to mimic absorption due to weakly allowed dipole forbidden transitions, indirect band gaps or disorder induced Urbach tails, in the case of $E_\mathrm{g} \approx E_\mathrm{n}$ and $\Gamma \ge E_\mathrm{n} - E_\mathrm{g}$ the absorption onset is dominated by the Lorentzian spectral shape and a pronounced high-energy absorption tail. Electronic band-band transitions at higher energy are usually spread over larger ranges of the Brillouin zone with slightly different energies and thus can be well described by Gaussian oscillators, which reflects the related inhomogeneous energy distribution of such transitions.

The parametrized total MDFs used consist of the Tauc-Lorentz model (Eq. (3), "TcLo"), two M0 critical point functions ("CPM0-1,2"),[30,31] two Gaussian oscillators ("Gaussian-1,2," where the second Gaussian is located almost outside the spectral range investigated but it was required to model the high-energy absorption), and a pole function (i.e.: an undamped harmonic oscillator, "Pol") in order to account for contributions of electronic transitions to ε_1 at energies higher than the spectral range investigated here

$$\tilde{\varepsilon}_\mathrm{total}(E) = \tilde{\varepsilon}_\mathrm{TcLo}(E) + \tilde{\varepsilon}_\mathrm{CPM0-1,2}(E) + \tilde{\varepsilon}_\mathrm{Gaussian-1,2}(E) + \tilde{\varepsilon}_\mathrm{Pol}(E). \tag{6}$$

2. Results

The individual MDF contributions are included in Fig. 4(b) as grey lines exemplarily for $x = 0.02$. It can be seen that the onset of absorption is dominated by the Tauc-Lorentz lineshape followed by a pronounced CPM0-type contribution. At higher energies, a much weaker CPM0 function along with Gaussian oscillators is used to describe the DF.

The energy parameters as a function of x of the individual MDF contributions are shown in Fig. 6(a). An almost continuous redshift within the entire composition range is observed as expected for the band gap and most of the other transition energies.[33] In the composition range of the structural phase separation, the slope changes slightly between

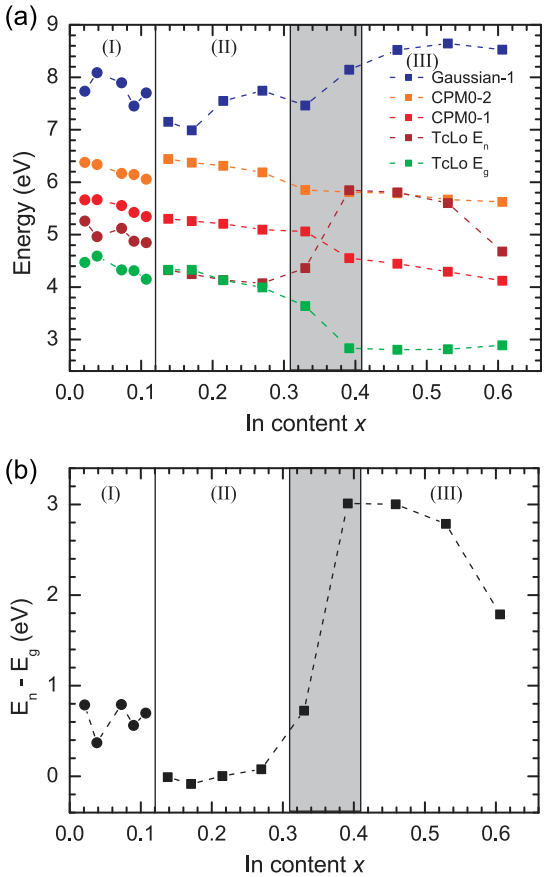

FIG. 6. (a) Energy parameters of the MDF contributions TcLo (E_g and E_n), CPM0-1, CPM0-2, and Gaussian-1. The uncertainty is in the order of some 100 meV, increasing from lower to higher energies. (b) Difference between both TcLo energy parameters E_g and E_n. In (a) and (b), squares and circles indicate the thin films grown on MgO and Al_2O_3 substrates, respectively. The grey marked area indicates for the sample with MgO substrate, the composition range of the transition from the single phase to the phase separated structure as significantly observable in the dielectric function spectra.

TABLE I. Energy parameters of the MDF used here (the uncertainty is in the order of the last digit given) and of absorption features reported in literature. Data refer to $x = 0.02/0.0$ and $x = 0.61/1.0$ for own results/literature data. In the first columns in the table, literature data for the direct band gap are given, also those conflated, which belong to different principle tensor elements of $\tilde{\varepsilon}$. Please consider also possible energy shifts between theory and experiments caused in general theoretical limitations.

	TcLoEg (eV)		TcLoEn (eV)		CPM0-1		CPM0-2		Gaussian-1	
x =	0.02/0	0.61/1	0.02/0	0.61/1	0.02/0	0.61/1	0.02/0	0.61/1	0.02/0	0.61/1
This work	4.5	2.9	5.3	4.7	5.7	4.1	6.4	5.6	7.8	8.5
Theory Refs. 2–6, 8, and 10	2.6…4.7	3.1…3.7				4	6.61…7.11	5	7.69	8
Experiment Refs. 10–16, 18,19, and 21	4.5…4.9	3.5…3.84				4.1…4.4				

the ranges (I and II) and (III) (grey marked area). Between the energies of the samples grown on Al_2O_3 (low x, range (I)) and MgO substrate (large x, range (II)), an energy shift is observed. The overall dependence $E_i(x)$ basically reflects the theoretical expectations,[2–9] previous experimental observations,[20,21] and also the behaviour of the lattice constants and phonon modes:[22] The smaller a-lattice constants for the film grown on MgO with respect to that on Al_2O_3 is reflected in higher transition energies, the slope change (grey marked area), and also the general increase of a with increasing x. The energy parameters of our MDF are compared with and assigned to those reported experimentally or predicted theoretically in Table I.

The TcLo contribution shows a further complex behaviour: while in the composition range (II), E_g and E_n are almost degenerated, in the phase separated composition range (III) $E_g \ll E_n$ (Fig. 6(b)). This behaviour nicely reflects the structural changes: as in the first case (II), the transition is dominantly Lorentzian with weak inhomogeneous broadening and disorder induced wide absorption tails, in the second case (III), the absorption tail becomes large. Further, the greater influence of the In 4d orbitals on the valence bands, possibly causing the indirect band gap or weakly allowed dipole forbidden direct band gap as discussed in Sec. I, contributes to the widening of the absorption tail. Wide sub-band gap absorption tails and indirect band gap absorption have also been observed for In_2O_3 thin films.[14,16,19] The film grown on Al_2O_3 (range (I)) is an exception of this general trend, showing a finite energy splitting, probably caused in the slightly inferior crystal quality compared to the film grown on MgO.

In order to further estimate the influence of disorder and indirect/forbidden transitions on weak sub-band gap absorption, we discuss the relative spectral weight contribution of the TcLo relative to the CPM0 contributions, shown spectrally integrated over the spectral ranges, where $(\varepsilon_2^{\mathrm{CPM0-1}} + \varepsilon_2^{\mathrm{CPM0-2}}) - \varepsilon_2^{\mathrm{TcLo}} < 0$, in Fig. 7. The TcLo dominates for the film grown on Al_2O_3 (range (I)) and in the composition range of the transition between the single phase (II) and phase separated (III) ranges (grey marked area). Within

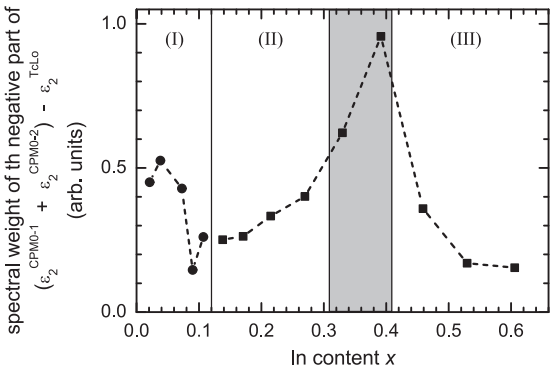

FIG. 7. Integrated spectral weight of the MDF contribution TcLo relative to CPM0-1 and CPM0-2 for the spectral range, where $(\varepsilon_2^{\mathrm{CPM0-1}} + \varepsilon_2^{\mathrm{CPM0-2}}) - \varepsilon_2^{\mathrm{TcLo}} < 0$ as a function of the composition. Squares and circles indicate the thin films grown on MgO and Al_2O_3 substrates, respectively. The grey marked area indicates for the sample with MgO substrate, the composition range of the transition from the single phase to the phase separated structure as significantly observable in the dielectric function spectra.

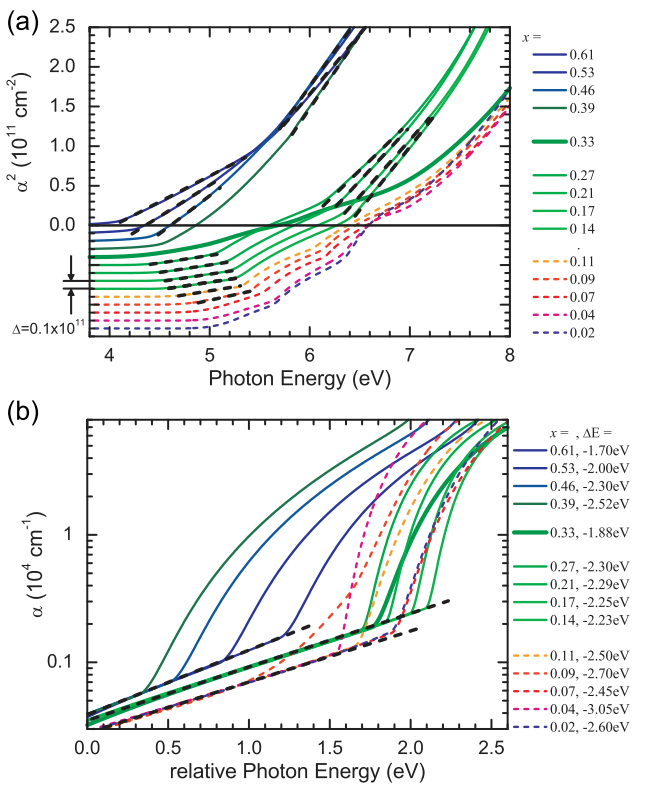

FIG. 8. Spectra of (a) the square of absorption coefficient α and (b) α in semi-logarithmic representation, calculated from the MDF. Solid and dashed coloured lines indicate the thin films grown on MgO and Al_2O_3 substrates, respectively. In (a), the spectra are shifted vertically against each other for clarity as indicated. In (b), the energy scale of each spectrum is shifted by the value indicated in the legend. The black dashed straight lines indicate spectral ranges, where α depends (a) parabolically and (b) exponentially on the energy.

the ranges (II) and (III), the electronic bands seem to be more defined resulting in more pronounced signatures of the parabolic CPM0 band absorption. This is demonstrated in Fig. 8(a), where α^2 in the spectral ranges around the two CPM0 contributions can be linearly approximated for these x-values. But nevertheless, also the exponential absorption tail is present for these compositions as can be seen by the linear shape of $\ln(\alpha)$ in Fig. 8(b). It should be noted that the linear approximation of $\ln(\alpha)$ yields within each of the composition ranges the same slope and increases from range (I) to (III) slightly, reflecting the in tendency decreasing overall spectral weight of the TcLo contribution.

IV. CONCLUSIONS

We have determined the DF of $(In_xGa_{1-x})_2O_3$ thin films in a wide spectral range from near-infrared to vacuum-ultraviolet and for a large composition range $x = 0.02 \ldots 0.61$. By comparison of the DF lineshape with theoretical predictions, we conclude that the electronic structure for $x < 0.3$ is dominantly that of monoclinic β-Ga_2O_3 and for $x > 0.4$ that of the cubic bcc-In_2O_3. In the intermediate composition range, the DF reveals strong signatures of rh-In_2O_3, but in Raman experiments, we observed the independent $InGaO_3$-II phase.[22] This coincidence may be by chance but could also reflect some similarities in the electronic properties of both phases.

ACKNOWLEDGMENTS

We acknowledge Michael Lorenz for XRD and Jörg Lenzner for EDX measurements of the thin films, Gabriele Ramm for the preparation of the PLD targets, Holger Hochmuth for thin film growth as well as Helena Franke and Chris Sturm for comments on the manuscript and valuable discussions. This work was supported within the framework of EFRE (SAB 100132251). C.K. was funded by the European Union and the Free State of Saxony.

[1]H. von Wenckstern, Z. Zhang, J. Lenzner, F. Schmidt, and M. Grundmann, Proc. Mater. Res. Soc. **1633**, 123–129 (2014).
[2]H. He, M. A. Blanco, and R. Pandey, Appl. Phys. Lett. **88**, 261904 (2006).
[3]K. Yamaguchi, Solid State Commun. **131**, 739 (2004).
[4]H. He, R. Orlando, M. A. Blanco, and R. Pandey, Phys. Rev. B **74**, 195123 (2006).
[5]S. Z. Karazhanov, P. Ravindran, P. Vajeeston, A. Ulyashin, T. G. Finstad, and H. Fjellvg, Phys. Rev. B **76**, 075129 (2007).
[6]F. Fuchs and F. Bechstedt, Phys. Rev. B **77**, 155107 (2008).
[7]P. Erhart, A. Klein, R. G. Egdell, and K. Albe, Phys. Rev. B **75**, 153205 (2007).
[8]A. Walsh, J. L. F. Da Silva, S.-H. Wei, C. Körber, A. Klein, L. F. J. Piper, A. DeMasi, K. E. Smith, G. Panaccione, P. Torelli, D. J. Payne, A. Bourlange, and R. G. Egdell, Phys. Rev. Lett. **100**, 167402 (2008).
[9]M. Ramzan, Y. Li, and R. Ahuja, Solid State Commun. **172**, 37 (2013).
[10]P. D. C. King, T. D. Veal, F. Fuchs, C. Y. Wang, D. J. Payne, A. Bourlange, H. Zhang, G. R. Bell, V. Cimalla, O. Ambacher, R. G. Egdell, F. Bechstedt, and C. F. McConville, Phys. Rev. B **79**, 205211 (2009).
[11]N. Ueda, H. Hosono, R. Waseda, and H. Kawazoe, Appl. Phys. Lett. **71**, 933 (1997).
[12]E. G. Víllora, M. Yamaga, T. Inoue, S. Yabasti, Y. Masui, T. Sugawara, and T. Fukuda, Jpn. J. Appl. Phys., Part 2 **41**, L622 (2002).
[13]M. Yamaga, T. Ishikawa, M. Yoshida, T. Hasegawa, E. G. Víllora, and K. Shimamura, Phys. Status Solidi C **8**, 2621 (2011).
[14]R. L. Weiher and R. P. Ley, J. Appl. Phys. **37**, 299 (1966).
[15]I. Hamberg, C. G. Granqvist, K. F. Berggren, B. E. Sernelius, and L. Engström, Phys. Rev. B **30**, 3240 (1984).
[16]M. Girtana and G. Folcher, Surf. Coat. Technol. **172**, 242 (2003).
[17]K. Irmscher, M. Naumann, M. Pietsch, Z. Galazka, R. Uecker, T. Schulz, R. Schewski, M. Albrecht, and R. Fornari, Phys. Status Solidi A **211**, 54 (2014).
[18]M. Rebien, W. Henrion, M. Hong, J. P. Mannaerts, and M. Flei-scher, Appl. Phys. Lett. **81**, 250 (2002).
[19]L. Miao, S. Tanemura, Y. G. Cao, and G. Xu, J. Mater. Sci. - Mater. Electron. **20**, S71 (2009).
[20]T. Oshima and S. Fujita, Phys. Status Solidi C **5**, 3113 (2008).
[21]L. Kong, J. Ma, F. Yang, C. Luan, and Z. Zhu, J. Alloys Compd. **499**, 75 (2010).
[22]C. Kranert, J. Lenzner, M. Jenderka, M. Lorenz, H. von Wenckstern, R. Schmidt-Grund, and M. Grundmann, J. Appl. Phys. **116**, 013505 (2014).
[23]Y. Lin-Hong, D. Hong-Xing, S. Zheng, S. Liao-Xin, S. Xue-Chu, and C. Zhang-Hai, Chin. Phys. Lett. **28**, 087803 (2011).
[24]B. Garcia-Domene, H. M. Ortiz, O. Gomis, J. A. Sans, F. J. Manjón, A. Muñoz, P. Rodríguez-Hernández, S. N. Achary, D. Errandonea, D. Martínez-García, A. H. Romero, A. Singhal, and A. K. Tyagi, J. Appl. Phys. **112**, 123511 (2012).
[25]C. Kranert, R. Schmidt-Grund, and M. Grundmann, Phys. Status Solidi RRL **8**, 554 (2014).
[26]H. von Wenckstern, Z. Zhang, F. Schmidt, J. Lenzner, H. Hochmuth, and M. Grundmann, CrystEngComm **15**, 10020 (2013).
[27]H. Fujiwara, *Spectroscopic Ellipsometry: Principles and Applications* (John Wiley and Sons, 2007).
[28]J. Jellison, L. A. Boatner, D. H. Lowndes, R. A. McKee, and M. Godbole, Appl. Opt. **33**, 6053 (1994).
[29]S. Shokhovets, L. Spieß, and G. Gobsch, J. Appl. Phys. **107**, 023509 (2010).
[30]S. Adachi, Phys. Rev. B **35**, 7454 (1987).
[31]H. Yoshikawa and S. Adachi, Jpn. J. Appl. Phys. **36**, 6237 (1997).
[32]G. E. Jellison and F. A. Modine, Appl. Phys. Lett. **69**, 2137 (1996); **69**, 371 (1996).
[33]Please note that $E_{\text{Gaussian}-1}$ has a large uncertainty caused in the position of this contribution at the very end of the investigated spectral range and, thus, strongly suffers from parameter correlation. Further, as mentioned above, $E_{\text{Gaussian}-2}$ is located almost outside and thus not accessible.
[34]Please note that in the following, we only discuss for this substrate type the composition range 0.11 because for larger In content, the ellipsometry data could not be modelled using a single phase model for the $(In_xGa_{1-x})_2O_3$ layer.